# Effects of bonding type and interface geometry on coherent transport through the single-molecule magnet $Mn_{12}$

Kyungwha Park[1], Salvador Barraza-Lopez[2], Víctor M. García-Suárez[3,4], and Jaime Ferrer[3]

[1]*Department of Physics, Virginia Polytechnic Institute and State University, Blacksburg VA, 24061*

[2]*School of Physics, Georgia Institute of Technology, Atlanta, GA 30332*

[3]*Departamento de Física & CINN, Universidad de Oviedo, 33007 Oviedo, Spain*

[4]*Department of Physics, Lancaster University, Lancaster, LA1 4YB, United Kingdom*

(Dated: June 20, 2013)

## Abstract

We examine theoretically coherent electron transport through the single-molecule magnet $Mn_{12}$, bridged between Au(111) electrodes, using the non-equilibrium Green's function method and the density-functional theory. We analyze the effects of bonding type, molecular orientation, and geometry relaxation on the electronic properties and charge and spin transport across the single-molecule junction. We consider nine interface geometries leading to five bonding mechanisms and two molecular orientations: (i) Au-C bonding, (ii) Au-Au bonding, (iii) Au-S bonding, (iv) Au-H bonding, and (v) physisorption via van der Waals forces. The two molecular orientations of $Mn_{12}$ correspond to the magnetic easy axis of the molecule aligned perpendicular [hereafter denoted as orientation (1)] or parallel [orientation (2)] to the direction of electron transport. We find that the electron transport is carried by the lowest unoccupied molecular orbital (LUMO) level in all the cases that we have simulated. Relaxation of the junction geometries mainly shifts the relevant occupied molecular levels toward the Fermi energy as well as slightly reduces the broadening of the LUMO level. As a result, the current slightly decreases at low bias voltage. Our calculations also show that placing the molecule in the orientation (1) broadens the LUMO level much more than in the orientation (2), due to the internal structure of the $Mn_{12}$. Consequently, junctions with the former orientation yield a higher current than those with the latter. Among all of the bonding types considered, the Au-C bonding gives rise to the highest current (about one order of magnitude higher than the Au-S bonding), for a given distance between the electrodes. The current through the junction with other bonding types decreases in the order of Au-Au, Au-S, and Au-H. Importantly, the spin-filtering effect in all the nine geometries stays robust and their ratios of the majority-spin to the minority-spin transmission coefficients are in the range of $10^3$ to $10^8$. The general trend in transport among the different bonding types and molecular orientations obtained from this study may be applied to other single-molecular magnets.



PACS numbers: 73.63.-b, 85.65.+h, 85.75.-d, 75.50.Xx

## I. INTRODUCTION

Advances in experimental techniques have led to a great number of experimental studies on electron transport through molecular junctions formed by single molecules bridged between electrodes or molecular monolayers adsorbed onto surfaces, using three-terminal set-ups or scanning tunneling microscopy (STM) measurements. Recently, molecular junctions based on single-molecule magnets (SMMs) connected to electrodes or monolayers of SMMs at surfaces, have been fabricated and their electron transport characteristics[1–6] have been measured, as well as their mechanical, electronic, and magnetic properties[7–13]. Electron transport through an SMM drew a lot of attention because of the intriguing interplay between its transport properties and the internal magnetic degrees of freedom, which is absent in transport through small organic molecules. An SMM consists of several transition metal ions interacting through organic or inorganic ligands via super-exchange interactions. The spin configuration of the ground state of an SMM is determined by a delicate balance among the super-exchange interactions of different strengths between the transition metal ions. Thus, the magnetic structure of an SMM must be taken into account in understanding its electron transport and other quantum properties. Recently, first-principles calculations of transport through an SMM were performed on a prototype SMM $Mn_{12}$ terminated with a thiol (-S) group within Au electrodes.[14–16] The calculations carried out in Refs.[14,15] suggest that the $Mn_{12}$ molecule can function as a spin filter with low bias voltage even with non-magnetic electrodes. Even though the $Mn_{12}$ is chemically bonded to the Au electrodes, the broadening of the relevant molecular orbitals is so small compared to its charging energy that the Kondo temperature is expected to be extremely low. In addition, these[14,15] and other calculations[16,17] demonstrate the importance of the internal magnetic degrees of freedom of the $Mn_{12}$ in electron transport, in contrast to typical quantum dots, regardless of the specific details of the coupling of the molecule to the electrodes.

Systematic studies on molecular junctions based on small organic molecules reveal that the current through the molecular junctions is highly sensitive to properties of interfaces between the molecules and electrodes because the interfaces determine the degree of the overlap between the molecular levels and conduction channels of the electrodes.[18–24] A thiol group is most commonly used to build a strong chemical link between the single molecules and the Au electrodes in molecular junctions. The conductance of such single-molecule

junctions is typically several orders of magnitude smaller than $G_0 = 2e^2/h$ (the conductance quantum). Binding of the S atoms to the hollow sites of the Au surface gives rise to different conductance (by a factor of about 2 to 3) from binding of the same S atoms to on-top sites of the Au surface.[21] Molecular junctions terminated with an amine (-N) group within Au electrodes reveal even lower conductance than those with a thiol group.[22] In order to increase conductance of molecular junctions, linker molecules including Au atoms[25] or isocyanide derivatives[26] were used between the single molecules and electrodes. In addition, recent experiments show that conductance through molecular junctions based on small single molecules can be enhanced to an order of $G_0$ by their direct bonding to the electrodes without a thiol group or any other linker molecules.[27,28] This enhancement is attributed to a strong coupling between the molecules and the electrodes, which places the transport in the transparent regime rather than in the tunneling regime.[28,29] However, corresponding systematic studies have not yet been carried out for electron transport through an SMM. In the case of quantum dots, the properties of interfaces are negligible in transport. However, for molecular junctions based on SMMs, the molecules are chemically bonded to the electrodes, and thus their transport properties can change with different interfaces even if the molecules are weakly coupled to the electrodes in the sense that the charging energy is much greater than the broadening of the relevant molecular levels. In this paper, we investigate how bonding types, interface geometries, and geometry relaxation influence transport characteristics of an SMM $Mn_{12}$ when it is bridged between Au electrodes.

An SMM $Mn_{12}$[30] consists of four inner $Mn^{4+}$ ions ($S = 3/2$) surrounded by eight outer $Mn^{3+}$ ions ($S = 2$) which are all antiferromagnetically coupled through O anions, as well as C and H atoms, as shown in Fig. 1. The dominant exchange interactions are between the inner $Mn^{4+}$ ions and the outer $Mn^{3+}$ ions.[31] In the ground state the magnetic moments of the four $Mn^{4+}$ ions are antiparallel to those of the eight $Mn^{3+}$ ions, such that the total spin becomes $S = 2 \times 8 - 3/2 \times 4 = 10$.[32–34] An SMM $Mn_{12}$ initially synthesized by Lis[30] consists of ligands which do not form direct chemical bonding to an Au surface. Thus, most transport experiments through an $Mn_{12}$ within Au electrodes were performed on systems where the $Mn_{12}$ molecules are chemically bonded to surfaces or electrodes via linker molecules such as a thiol group,[1,3,5] or physically adsorbed onto surfaces or electrodes without any linker molecules.[2] To form direct Au-S bonding, some of the original ligands of the $Mn_{12}$ molecules[30] were substituted by S-containing ligands, or the $Mn_{12}$ molecules were deposited

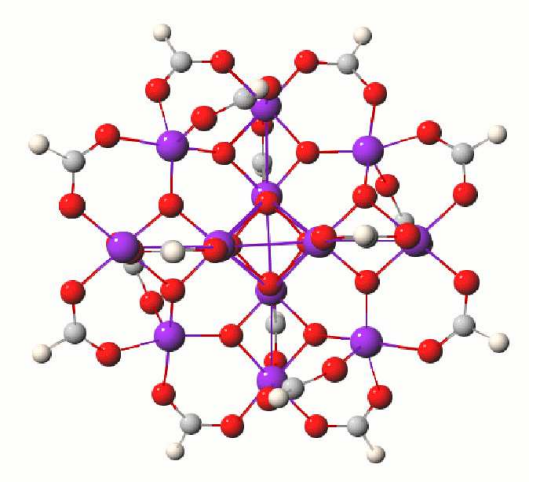

FIG. 1: (Color online) Top view of an isolated $Mn_{12}$ molecule: Mn (purple), O (red), C (gray), H (white). The ground-state spin is $S = 10$ or the magnetic moment is 20 $\mu_B$.

onto an Au surface that was initially functionalized with S-containing alkane chains.[5] So far, the measured electric current through an $Mn_{12}$ molecule or its derivative in various experiments is in the range of 1 pA to 100 pA at bias voltage of a few tens of mV.[1,2,5] Compared to binding a small organic molecule to Au electrodes through a thiol or amine group, binding an $Mn_{12}$ to Au electrodes via linker molecules bears the following differences: (a) an $Mn_{12}$ has much more binding sites to the linker molecules, and (b) the orientation of an $Mn_{12}$ relative to the electrodes is, to a great extent, determined by binding sites of the linker molecules to the $Mn_{12}$, rather than their binding sites to the electrodes.

Full control of the properties of interfaces is extremely difficult to achieve in molecular junctions and tunneling measurements using STM or scanning tunneling spectroscopy (STS).[20,22–24,27,28] Thus, in transport experiments, for a given bonding type, several binding sites are plausible, and hundreds of fabricated samples of the bonding type give rise to a histogram of conductance for given gate voltage or a series of current-voltage curves. In the present study, we take into account five different bonding types between an $Mn_{12}$ and Au electrodes, and for each bonding type, some representative interface geometries are examined. Even though we do not simulate all possible configurations of the interface that may be realized in fabricated samples for a given bonding type, the general trend in our calculated transport properties will elucidate the effects of linker group, molecular orientation, and geometry relaxation, as well as the effectiveness of different bonding types and interface

geometries in transport through an $Mn_{12}$ and other SMMs.

In this work, we consider an $Mn_{12}$ molecule bridged between Au(111) electrodes (two-terminal set-up) via nine different ways (Fig. 2), and investigate their current-voltage characteristics using the density-functional theory (DFT) and the nonequilibrium Green's function method (NEGF). The nine different ways can be categorized according to their bonding types: (i) Au-S bonding, (ii) Au-C bonding, (iii) Au-Au bonding, (iv) Au-H bonding, and (v) physisorption through van der Waals forces. DFT does not fully capture the nature of van der Waals forces where the orbitals considered do not overlap. We note, however, that if molecular orbitals do not overlap with the orbitals of electrodes at a molecular junction, the transport properties of the junction belong to the tunneling regime. A recent study reveals that first-principles calculations based on DFT and NEGF provide qualitative features of transport in such a regime.[35] For example, when a Pt break junction becomes broken with vacuum between the electrodes, a first-principles calculation showed exponentially decaying conductance as a function of distance between the electrodes.[35] This result suggests that our methodology can be used to understand the transport in the case of physisorption, although the physical mechanism in our case differs from that in the broken junction. In the present calculations, we consider two molecular orientations relative to the electrodes: when the magnetic easy axis of the $Mn_{12}$ is normal [orientation (1)] or parallel [orientation (2)] to the transport direction, the $z$ axis, as shown in Fig. 2. The structure of the $Mn_{12}$ dictates that in the orientation (1) one linker molecule can be attached to each electrode without significantly deforming the $Mn_{12}$, while in the orientation (2), two linker molecules are possibly accommodated for each electrode without much distortion. As illustrated in Fig. 2, the nine different interface geometries are named based on the following rule. Adapted from the notations used in Refs.[14,15], we refer to the orientation (1) as Geo 1, and to the orientation (2) as Geo 2. For each interface geometry, the orientation of an $Mn_{12}$ is first specified, then the type of adsorption (either chemical or physical) is given. For chemical bonding, the type of bonding and the name of the linker group are noted, while for physisorption, whether linker molecules are placed or not is stated. For example, Geo 1:Au-$(SC_3H_6)_2$-hollow [Fig. 2(a)] denotes an interface geometry with the $Mn_{12}$ in the orientation (1) and the linker molecule $(SC_3H_6)_2$ bonded to the hollow sites of the electrodes via Au-S bonding. We will first outline our model and computational method. Then we will discuss the interface geometries in detail, and the effects of geometry relaxation, molecular orientation, bonding type, and

linker group on transport properties of the $Mn_{12}$. A brief conclusion will follow.

## II. COMPUTATIONAL METHOD AND MODEL

We use the quantum transport code SMEAGOL[36,37] interfaced with the DFT code SIESTA[38]. The Au electrodes are treated semi-infinitely using SIESTA. The scattering region consists of the $Mn_{12}$, linker molecules, and six flat Au atomic layers on each side of the $Mn_{12}$ ($6 \times 6$ surface atoms per layer), as shown in Fig. 2. Even if the number of the Au atomic layers increases from six to nine on each side of the $Mn_{12}$, the transmission probability does not change at all. This was tested and confirmed for the interface geometry with the Au-C bonding [Geo 1:Au-$(C_3H_6)_2$, Fig. 2(c)], where the broadening of the relevant molecular level turns out to be the largest among the interface geometries considered. The electronic structures of the electrodes and scattering region are calculated within the spin-polarized Perdew-Burke-Ernzerhopf (PBE) generalized-gradient approximation (GGA)[39], using SIESTA. We generate Troullier-Martins pseudopotentials[40] for Au, Mn, S, O, C, and H with scalar relativistic terms and core corrections except for H. We also build corresponding basis sets of the elements using the scheme presented in Ref. [41]. For the Mn basis set, $3p$ orbitals as a semicore are required in order for the molecular orbital levels of an isolated $Mn_{12}$ to be comparable to those obtained from all-electron calculations[42]. With these pseudopotentials and basis sets, self-consistent DFT calculations including spin-orbit coupling[37] are performed for an isolated $Mn_{12}$. Using a modified version[37] of SIESTA, we obtain the total magnetic moment of 20 $\mu_B$ and the magnetic anisotropy barrier of 66.4 K,[14]. This is in good agreement with experiment[33] and with the barrier[43,44] computed using the DFT code VASP[45]. To reduce the computational cost, a small Au basis set of a single $s$ orbital is used for transport calculations, while a large Au basis set of both $d$ and $s$ orbitals is used for geometry relaxation. The transmission at the Fermi level in Au is dominated by the $s$ states because the $d$ orbital levels are well below the Fermi level. It is checked that in the scattering region, the density of states projected onto Mn $d$ orbitals with the large Au basis set is fairly similar to that with the small Au basis set, which justifies the utilization of the small Au basis set in the transport study. For a given interface geometry, the distance $d$ between the electrodes was determined such that all of the terminating atoms from the linker molecules (such as S, C, or Au atoms) are bonded to the lowest-energy sites of the the Au slab with reasonable bond

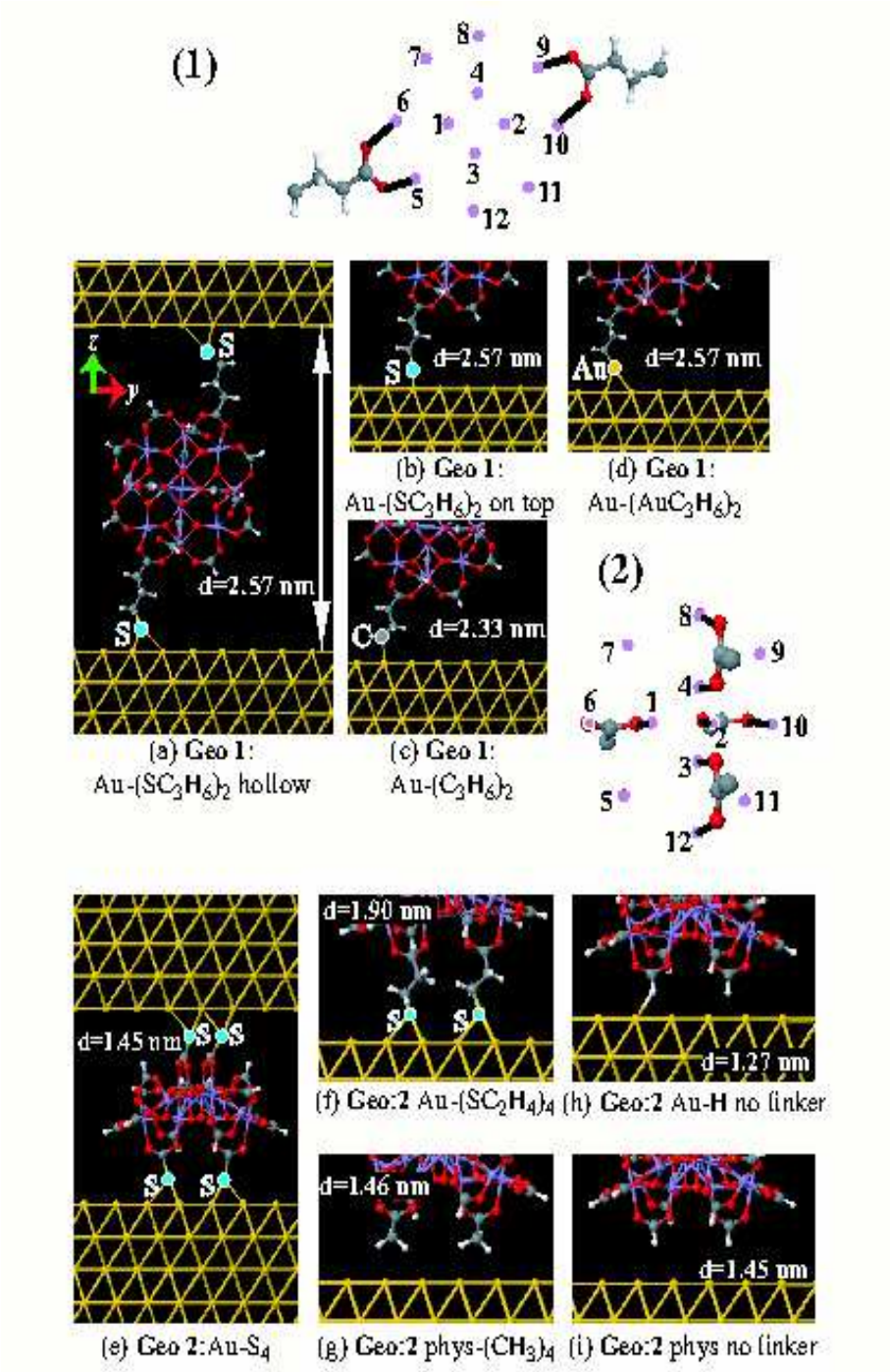


FIG. 2: (Color online) The nine geometries of the scattering region with different bonding types and linker groups. Not all of the Au atomic layers are shown. (a), (b), (e), (f): Au-S bonding with different linker molecules and in the orientations (1) and (2). (c): Au-C bonding, (d): Au-Au bonding, (g) and (i): physisorption with and without linker molecules, respectively. (h): Au-H bonding. On the top and in the middle, the positions of the twelve Mn ions in relation to the binding sites for the linker molecules are labeled for the orientations (1) and (2), respectively.

lengths. For example, for the Au-S bonding, the distance $d$ was obtained from an optimum bond length between a S-terminated alkane chain and the hollow site of a small Au cluster. In constructing the initial geometry of the scattering region, each component of the region, such as the electrodes, the $Mn_{12}$, and the linker molecules, are separately optimized in advance. The largest force is found at the interface between the linker molecules and the electrodes.[43] Thus, the geometry relaxation with a fixed $d$ allows the linker molecules and the $Mn_{12}$ to relax further and lowers the force at the interface. Prior to the transport calculations, all of the geometries of the scattering region or interface geometries considered are relaxed with a fixed distance $d$ between the electrodes, using `SIESTA`, until the magnitude of the maximum force exerted on the atoms becomes less than 0.1 eV/Å, unless stated otherwise.

To avoid any quantum confinement effects,[36] for the scattering region, periodic boundary conditions are applied in the transverse directions and $3 \times 3 \times 1$ $k$-points are sampled. The retarded Green function for the scattering region, $G^{\mathrm{R}}_{\mathrm{EM}}$, has the form of $[\epsilon^{+} S_{\mathrm{EM}} - H_{\mathrm{EM}} - \Sigma^{\mathrm{R}}_{\mathrm{L}} - \Sigma^{\mathrm{R}}_{\mathrm{R}}]^{-1}$, where $S_{\mathrm{EM}}$ and $H_{\mathrm{EM}}$ are the overlap and Hamiltonian matrices for the scattering region, respectively.[36] Here $\Sigma^{\mathrm{R}}_{\mathrm{L}}$ and $\Sigma^{\mathrm{R}}_{\mathrm{R}}$ are self-energies arising from the interactions of the $Mn_{12}$ with the left and right electrodes, respectively. These self-energies depend on energy $E$ and $k$ vector, and they are obtained from spin-polarized calculations of retarded surface Green functions for the electrodes which are computed using the scheme developed in Ref.[46]. The initial magnetic moment of the scattering region is set to 20 $\mu_B$. Interactions with phonons or additional electron correlations such as on-site Coulomb repulsion (Hubbard-like $U$ term) are not taken into account. The density matrix of the scattering region is self-consistently solved within the NEGF formalism until it converges. After the convergence of the density matrix, the total magnetic moment slightly increases, such as 20.3 $\mu_B$ for Geo 1:Au-$(SC_3H_6)_2$-hollow, due to a small amount of spin polarization in the Au atomic layers caused by the $Mn_{12}$. Then the transmission $T(E, V_b)$ at low bias voltage $V_b$ is calculated as follows:

$$T(E, V_b) \;=\; \mathrm{Tr}[\Gamma_L \, G^{\mathrm{R}\dagger}_{\mathrm{EM}} \, \Gamma_R \, G^{\mathrm{R}}_{\mathrm{EM}}](E, V_b), \tag{1}$$

where $\Gamma_L$ and $\Gamma_R$ denote the broadening of molecular levels induced by coupling to the left and right electrodes. Accurate calculations of $T(E, V_b)$ require high resolution in energy $E$ (such as 7$\mu$eV for very sharp transmission peaks) due to the weak coupling between the $Mn_{12}$

and the electrodes. Since the electrodes are treated semi-infinitely and periodic boundary conditions are employed, the transmission coefficients are obtained after their integration over the $k$-points. The current $I$ as a function of $V_b$ is obtained from

$$I(V_b) = \frac{e}{h} \int dE \; T(E, V_b) \, [f(E + eV_b/2) - f(E - eV_b/2)], \tag{2}$$

where $f(E + eV_b/2)$ and $f(E - eV_b/2)$ are the Fermi-Dirac distribution functions of the left and right electrodes. The electronic temperature used is 10 K.

## III. RESULTS AND DISCUSSION

We examine the nine interface geometries (Fig. 2) leading to the five bonding types and two molecular orientations that were discussed in Sec. I. Their molecular orientations, linker groups, bonding types, binding sites, and distances $d$ between the electrodes are listed in Table 1.

### A. Interface geometries considered

In the Au-S bonding, four interface geometries are considered: Fig. 2(a), (b), (e), and (f). In Fig. 2(a), Geo 1:Au-$(SC_3H_6)_2$-hollow, one $SC_3H_6$ linker molecule is bonded to each Au electrode, where the S atom is adsorbed at the hollow sites of the flat Au surface. For a fixed distance $d$, after the geometry relaxation, this geometry bears the shortest distances between the S and Au surface atoms in the range of 2.52 to 2.82 Å. If the S atom is bonded to the on-top site of the Au surface [Geo 1:Au-$(SC_3H_6)_2$-ontop, Fig. 2(b)], the total energy increases by 0.094 eV compared to the hollow-site case, and the shortest distance between the S and Au atoms becomes 1.92 Å. In Fig. 2(e) and (f), two S linker atoms [Geo 2:Au-$S_4$] or two $SC_2H_4$ linker molecules [Geo 2:Au-$(SC_2H_4)_4$] are bonded to the hollow sites of the surface of each electrode. For these two geometries the shortest distances between the S and Au atoms are in the range of 2.52 to 2.68 Å.

Our study of the Au-C bonding was motivated by recent measurements on the conductance of a molecular junction based on benzene directly bonded to Pt electrodes.[27] It is prevalent that chemical bonding between a metallic surface and C atoms is difficult to achieve under ordinary conditions, especially between an Au surface and C atoms. However,

the direct Au-C bonding does occur in a few exceptional cases, such as isocyanide derivatives adsorbed on Au surfaces.[47,48] In the geometry with the Au-C bonding [Geo 1:Au-$(C_3H_6)_2$, Fig. 2(c)], one $C_3H_6$ linker molecule is adsorbed at the on-top site of each electrode, and the shortest distance between the Au and outermost C atoms is 2.28 (2.37) Å for the left (right) linker molecule. The study of the Au-Au bonding was inspired by an experimental effort to increase conductance through small molecules using Au-Au bonding.[25] In the geometry with the Au-Au bonding [Geo 1:Au-$(AuC_3H_6)_2$, Fig. 2(d)], one $AuC_3H_6$ linker molecule is bonded to the hollow sites of each electrode, and the shortest distances between the Au surface and the Au atoms from the linker molecules are in the range of 2.73 to 2.79 Å.

The study of the geometries with physisorption and without linker molecules, was motivated by the transport measurement through the $Mn_{12}$ without any linker molecules[2]. We consider such geometries in the orientation (2). In the geometry with the Au-H bonding [Geo 2:Au-H-no-linker, Fig. 2(h)], no linker molecules are placed between the $Mn_{12}$ and the electrodes. However, the short distance $d$ in that geometry allows Au-H bonding to be initially formed at four different locations. We choose one of the four Au-H bonding distances in its initial geometry to be slightly shorter than the three distances, and then upon geometry relaxation, only one Au-H bonding remains effective as shown in Fig. 2(h). In the case of physisorption, two geometries are considered: Figs. 2(g) and (i). In Fig. 2(g), Geo 2:phys-$(CH_3)_4$, two $CH_3$ linker molecules are attached to each side of the $Mn_{12}$. Upon geometry relaxation (with a fixed $d$ until the magnitude of the maximum force is less than 0.1 eV/Å), in this geometry, the shortest distance between the Au and the C atoms from the linker molecules is 2.41 Å, which is long enough such that chemical bond is not formed between the linker molecules and the electrodes. In Fig. 2(i), Geo 2:phys-no-linker, no linker molecules are placed between the $Mn_{12}$ and the electrodes, and the Au surface atoms are well separated from the H atoms from the $Mn_{12}$ in the range of 2.97 to 3.10 Å. Thus, no chemical bond is formed between the electrodes and the $Mn_{12}$ in this geometry, either. The geometry of Geo 2:phys-no-linker was built from the optimized geometry of Geo 2:Au-H-no-linker with an increased distance $d$. Hereafter, when a particular bonding type is discussed, its corresponding binding site is also implicitly assumed.

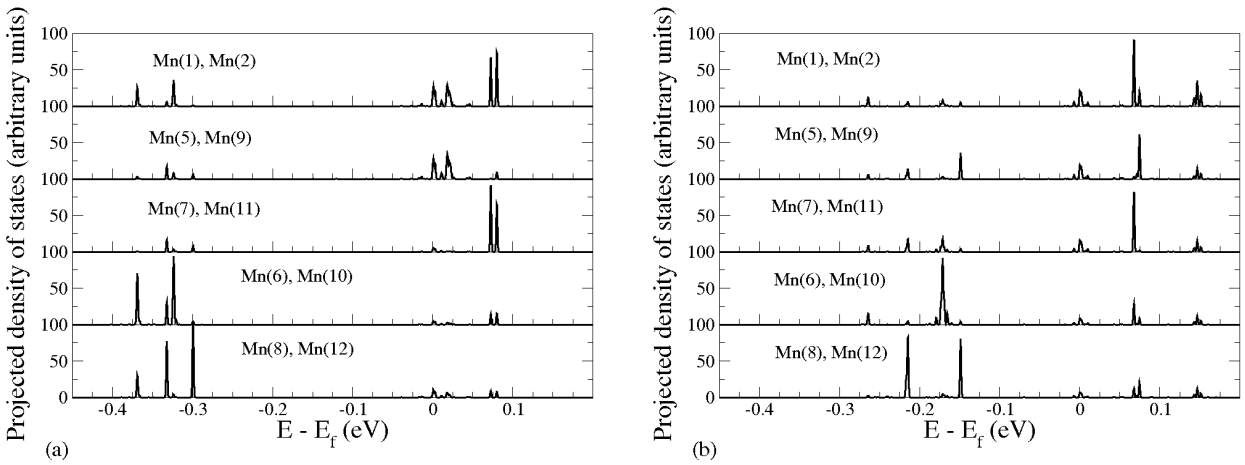


FIG. 3: Majority-spin density of states projected onto the Mn $d$ orbitals of the (a) initial and (b) optimized geometries, Geo 1:Au-$(SC_3H_6)_2$-hollow. Refer to Fig. 2 for numbering of the Mn sites. The densities of states for Mn(3) and Mn(4) sites are the same as those for Mn(1) and Mn(2).

### B. Effect of geometry relaxation

For an isolated $Mn_{12}$ molecule in the gas phase, without the on-site Coulomb repulsion $U$, our DFT calculations using `SIESTA` show that the energy gap between the highest occupied molecular orbital (HOMO) and the lowest unoccupied molecular orbital (LUMO) levels is 0.38 eV. Since the $Mn_{12}$ has a high magnetic moment of 20 $\mu_B$ in the ground state, both the HOMO and LUMO arise from the majority-spin Mn $d$ orbitals. This feature of the HOMO and LUMO does not change with inclusion of a proper value of the $U$ term, although the HOMO-LUMO energy gap increases with the $U$ term. This was shown in previous DFT+U calculations[44,49], in contrast to the result discussed in Ref.[16]. Such a characteristic of the HOMO and LUMO was also earlier revealed by all-electron DFT calculations[42], and it was indirectly demonstrated in experiments on locally charged $Mn_{12}$ molecules[50,51].

When an $Mn_{12}$ is bridged between the electrodes in the orientation (1), the $S_4$ symmetry of an isolated $Mn_{12}$ is broken and the molecular levels in the interface show approximately twofold symmetry. In addition, the magnetic easy axis of the $Mn_{12}$ is slightly tilted from the axis perpendicular [$x$ axis, Fig. 2(a)] to the transport direction, in order to allow the linker molecules to be bonded to the electrodes. Furthermore, geometry relaxation at a fixed $d$ renders some noticeable changes in the molecular levels. To compare the molecular levels before and after the geometry relaxation, we examine the geometry Geo 1:Au-$(SC_3H_6)_2$-

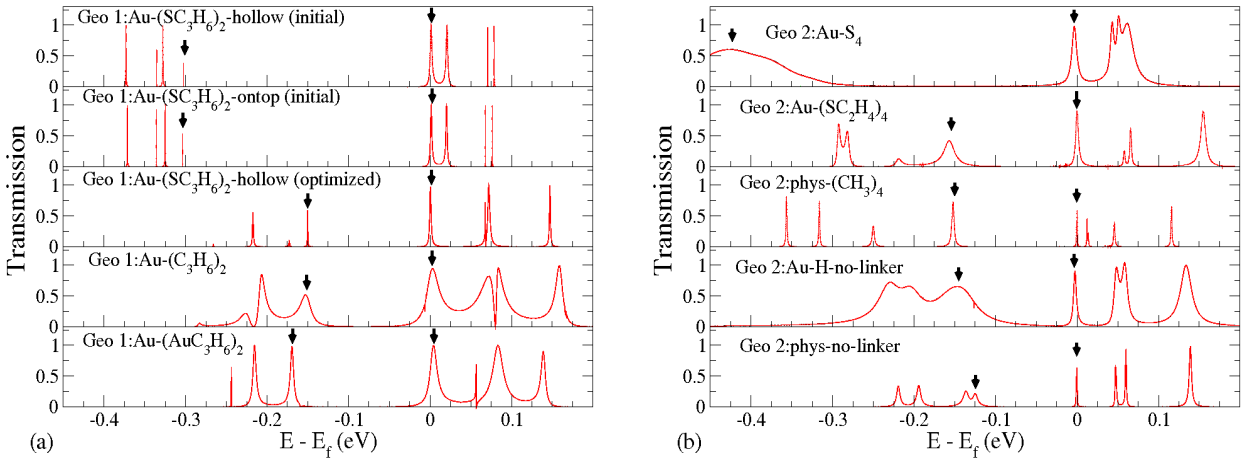


FIG. 4: (Color online) (a) Majority-spin transmission $T(E,0)$ at zero bias as a function of energy $E$ relative to the Fermi level $E_f$ for the five interface geometries with the orientation (1), and (b) for the five geometries with the orientation (2). The arrows indicate the transmission peaks associated with the HOMO and LUMO levels of the $Mn_{12}$.

hollow. For its initial geometry, the HOMO and LUMO levels of the Mn $d$ orbitals, are separated by 0.3 eV, which is similar to the HOMO-LUMO energy gap of 0.38 eV for the isolated $Mn_{12}$. With the geometry optimization, the Mn $d$ orbital levels right below the Fermi level $E_f$ approach toward $E_f$, but the Mn $d$ levels right above $E_f$ become split (Fig.3). As a result, the separation between the HOMO and LUMO levels reduces to 0.15 eV. The HOMO level is located near $-0.15$ eV, while the LUMO level is near $E_f$ [Fig. 3(b)] (this is due to some charge transfer from the Au electrodes to the $Mn_{12}$[43]). The same kind of shift is expected for the rest of the geometries considered in the orientation (1). Now when an $Mn_{12}$ is bridged between the electrodes in the orientation (2), the $S_4$ symmetry is by large preserved in the molecular levels in the interface. If the distance $d$ is not too short, the geometry relaxation will shift the molecular levels for geometries in the orientation (2) as well. One exception is Geo 2:Au-$S_4$, where a combination of the strong Au-S bonding with the short distance $d$ prevents the $Mn_{12}$ and the four S atoms from being significantly rotated or stretched/compressed with geometry relaxation.

We discuss the effect of geometry relaxation on $T(E,0)$. Similarly to the effect on the molecular levels, the geometry relaxation gives rise to a upward shift in the transmission peaks right below $E_f$ and more spread peaks right above $E_f$, as shown in the first and the third panels of Fig. 4(a) from the top. According to our calculations, the current is carried

via the LUMO level of the $Mn_{12}$, and thus the broadening of the LUMO level is relevant to the current-voltage characteristics. Without contributions from interactions with phonons, in resonance, the individual transmission peak centered at $E_i$ for given $V_b$ (for a single conductance channel) is solely described by the broadening of the corresponding molecular level as follows:[52,53]

$$T(E, V_b) = \frac{\Gamma_1(E_i, V_b)\Gamma_2(E_i, V_b)}{4(E - E_i)^2 + \Gamma(E_i, V_b)^2}, \tag{3}$$

where $\Gamma_1(E_i, V_b)$ and $\Gamma_2(E_i, V_b)$ are the broadening of the $i$th molecular level caused by the left and right electrodes, respectively, and they are determined by full widths at half maximum of the transmission peak centered at $E_i$. Here $\Gamma(E_i, V_b)$ is the average broadening given by $(\Gamma_1(E_i, V_b) + \Gamma_2(E_i, V_b))/2$. (Notice that for symmetric coupling, $\Gamma_1 = \Gamma_2$, Eq. (3) implies that $T$ becomes unity at $E = E_i$.) The orbital broadening $\Gamma_{1,2}(E_i, V_b)$ is related to the hopping integral $t_{1,2}$ (between the electrodes and the $Mn_{12}$) as $\pi t_{1,2}^2 \rho(E_i)$, where $\rho(E_i)$ is the density of states at the $i$th level.[54] The values of $t_{1,2}$ and $\rho(E_i)$ depend on bonding types and binding sites. We compute the values of $\Gamma_1$ and $\Gamma_2$ from fitting the transmission peaks to Eq. (3). For Geo 1:Au-$(SC_3H_6)_2$-hollow, the geometry relaxation reduces the value of $\Gamma_{\rm LUMO}$ from 0.0028 to 0.0020 eV, while it enhances the value of $\Gamma_{\rm HOMO}$ from $2.6\times10^{-5}$ to $5.0\times10^{-4}$ eV, as listed in Table 1. Since the value of $\Gamma_{\rm LUMO}$ decreases to a small degree with the geometry relaxation, a slightly lower current flows through the relaxed junction than via the initial one (the topmost left panel of Fig. 5). Similar behavior is expected for the rest of the geometries. Henceforth, we discuss optimized interface geometries only, unless specified otherwise.

### C. Effect of molecular orientation

For the interface geometries with the orientation (1), Fig. 2(a), (b), (c), and (d), the linker molecules are closer to the Mn(5), Mn(6), Mn(9), and Mn(10) sites than the rest of the eight Mn sites, as illustrated in Fig. 2. Among the former four Mn sites, the Mn(5) and Mn(9) sites predominantly contribute to the LUMO of the $Mn_{12}$ [Fig. 6(a)], as well as to some degree to the HOMO [Figs. 3(b) and 6(b)]. Notice that the HOMO and LUMO arise from the majority-spin Mn $d$ orbitals. A much greater contribution to the HOMO arises from the Mn(8) and Mn(12) sites [Fig. 6(b)], but these sites are not as close to the

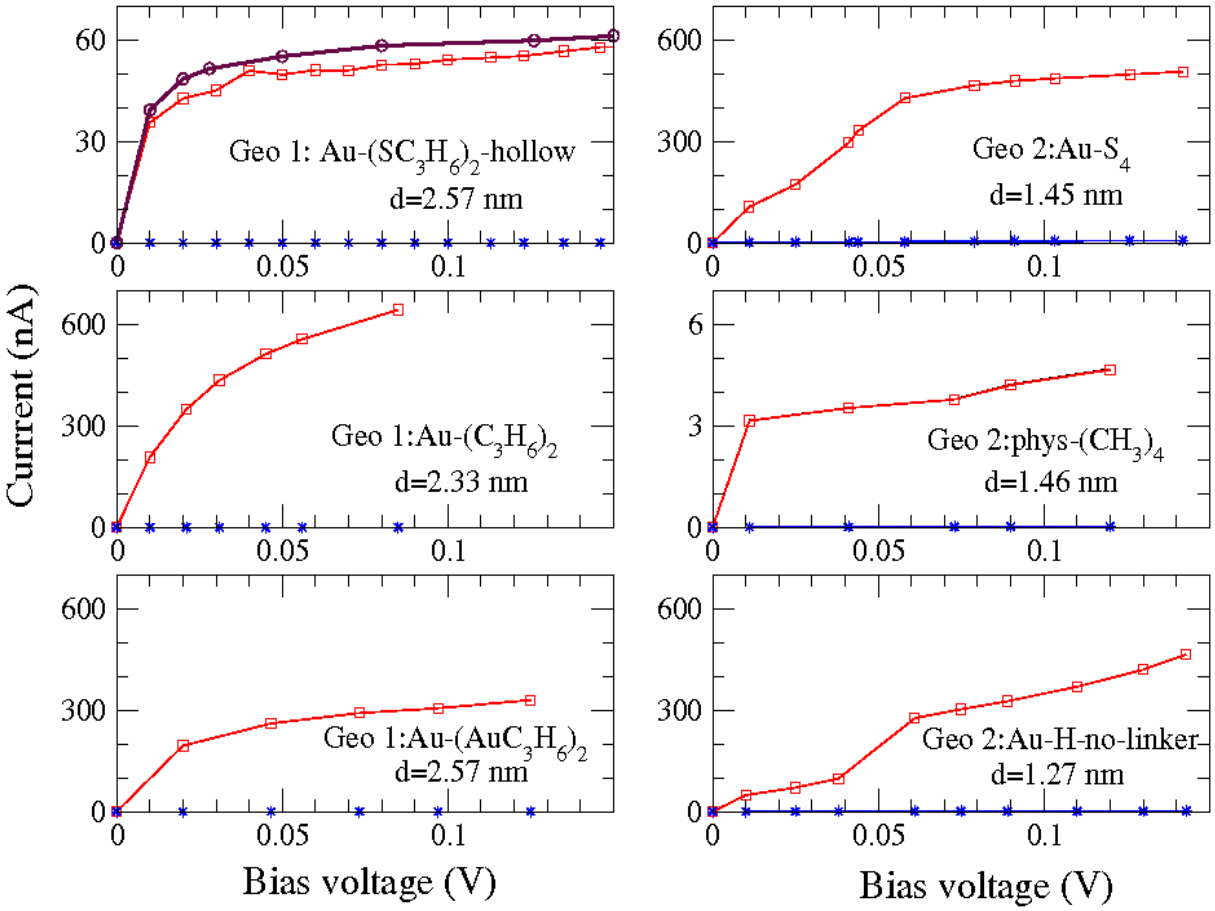


FIG. 5: (Color online) Current-voltage ($I-V$) characteristics for six interface geometries: majority-spin contribution (red box), minority-spin contribution (blue star). The topmost left panel shows $I-V$ curves for both the initial (brown circle) and the optimized geometries Geo 1:Au-$(SC_3H_6)_2$-hollow (red box). Note that Geo 1:Au-$(SC_3H_6)_2$-hollow and Geo 2:phys-$(CH_3)_4$ have different vertical scales from the rest of the geometries.

linker molecules as the former four sites. Thus, for the geometries with the orientation (1), the broadening of the LUMO level is expected to be somewhat larger than that of the HOMO level, as shown in Table 1 and Figs. 3(b), 4(a), and 7. For the geometries with the orientation (2), in the case of chemisorption, Fig. 2(e), (f), and (h), the linker molecules are in a closer proximity to the Mn(1), Mn(2), Mn(3), Mn(4), Mn(6), Mn(8), Mn(10), and Mn(12) sites, than to the other four Mn sites, as shown in Fig. 2. The Mn(6), Mn(8), Mn(10), and Mn(12) sites predominantly contribute to the HOMO [Fig. 6(d)] rather than the LUMO [Fig. 6(c)], and so the broadening of the HOMO level is much larger than that of the LUMO level [Table 1 and Fig. 4(b)]. In Fig. 4(b), the transmission peak associated

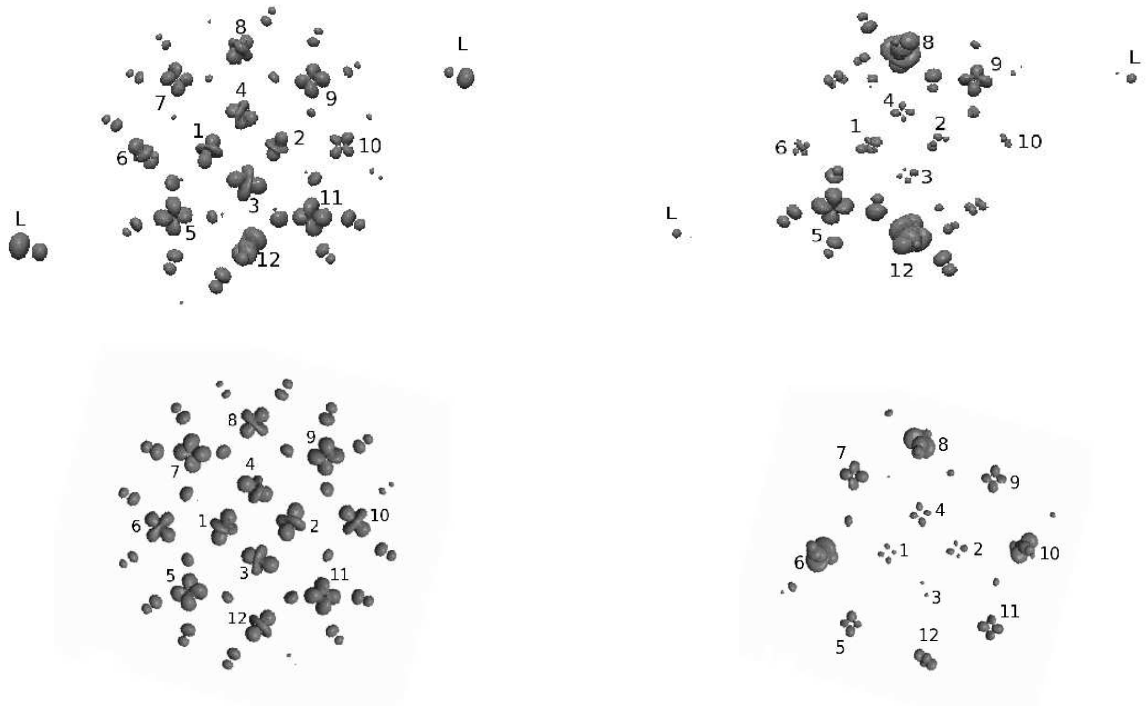


FIG. 6: Spatially resolved density of states (DOS) projected onto (a) the LUMO and (b) HOMO for Geo 1:Au-$(C_3H_6)_2$, and onto (c) the LUMO and (d) HOMO for Geo 2:Au-H-no-linker. The LUMO and HOMO originate from the majority-spin Mn $d$ orbitals. The criterion of the isosurface shown is $2.0 \times 10^{-3}$ electrons/$a_B^3$, where $a_B$ is the Bohr radius. The numbering of the Mn ions is based on Fig. 2. The blobs far away from the core of the $Mn_{12}$ (marked by L) in (a) and (b) arise from the linker molecules.

with the HOMO level for Geo 2:Au-$S_4$ (Geo 2:Au-H-no-linker), is very broad because it corresponds to four (two) molecular levels broadened right below $E_f$ including the HOMO level. In the case of physisorption, Figs. 2(g) and (i), the Mn(6), Mn(8), Mn(10), and Mn(12) sites are much closer to the electrodes than the Mn(5), Mn(7), Mn(9), and Mn(11) sites. The HOMO originates mainly from the former four Mn $d$ orbitals, while the LUMO comes from the latter four Mn $d$ orbitals. Thus, for the geometries in the orientation (2), either in the case of chemisorption or physisorption, the broadening of the HOMO level is expected to be much larger than that of the LUMO level [Table 1 and Fig. 4(b)].

Now we compare the level broadening for the geometries in the orientation (1) to that in the orientation (2), for a given bonding type and fixed distance $d$. For this comparison, we examine the following three geometries with the Au-S bonding: one geometry in the

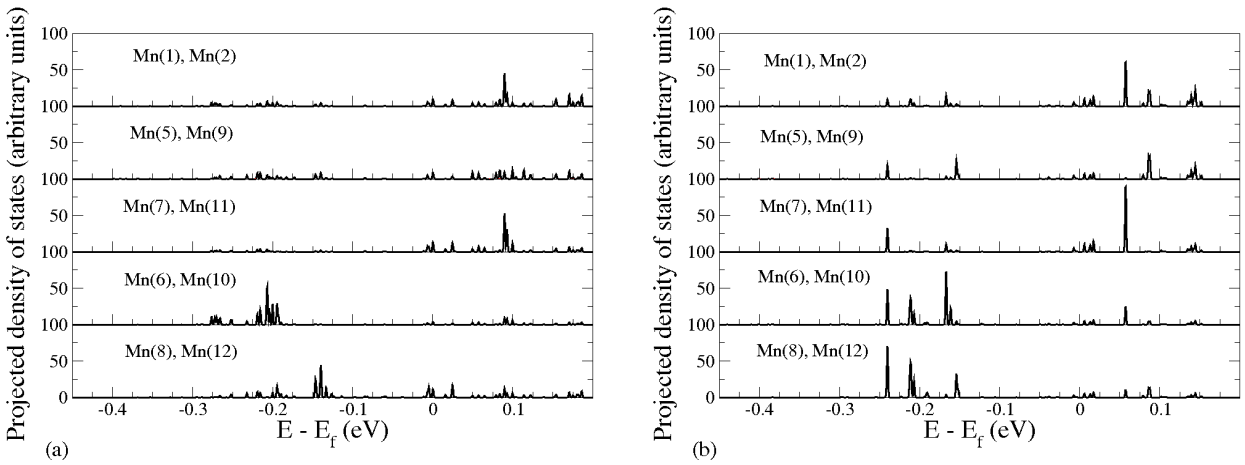


FIG. 7: Majority-spin density of states (DOS) projected onto Mn $d$ orbitals for (a) Geo 1:Au-$(C_3H_6)_2$ and (b) Geo 1:Au-$(AuC_3H_6)_2$. Refer to Fig. 2 for numbering of the Mn ions. The densities of states for Mn(3) and Mn(4) sites are the same as those for Mn(1) and Mn(2) sites.

orientation (1), Geo 1:Au-$(SC_3H_6)_2$-hollow, and two geometries in the orientation (2), Geo 2:Au-$S_4$ and Geo 2:Au-$(SC_2H_4)_4$. The distance $d$ in the former geometry, 25.73 Å, is much longer than those for the latter two geometries. Thus, we extrapolate to find the broadening of a corresponding geometry in the orientation (2) with $d$=25.73 Å. The $Mn_{12}$ and the linker molecules play the role of a potential barrier in the electron transport, and so the broadening of the relevant molecular levels decays exponentially as a function of $d$. Thus, we apply $\Gamma_{\rm LUMO}=C_1\exp(-C_2 d)$, where $C_1$ and $C_2$ are positive constants, to the two geometries in the orientation (2). Extracting the values of $C_1$ and $C_2$, we find that the extrapolated value of $\Gamma_{\rm LUMO}$ for $d$=25.73 Å is 0.0015 eV, which is less than the actual value of $\Gamma_{\rm LUMO}$ for the first geometry in the orientation (1), 0.0020 eV. When the same logic is applied to the HOMO level, the extrapolated value of $\Gamma_{\rm HOMO}$ for such a geometry becomes 0.0069 eV,[55] which is much greater than the actual value of $\Gamma_{\rm HOMO}$ for the first geometry, 0.00050 eV. Consequently, for a given bonding type and fixed distance $d$, the broadening of the LUMO (HOMO) level for geometries with the orientation (1) is more (less) pronounced than that with the orientation (2). Combining this result with the finding that the LUMO level broadens more than the HOMO level for the geometries with the orientation (1) and the opposite holds for those with the orientation (2), we reach the following conclusion. Although more statistics is desirable and other bonding types can be tested, our calculations indicate that as long as the current flows through the LUMO level, (for a given $d$ and bonding type)

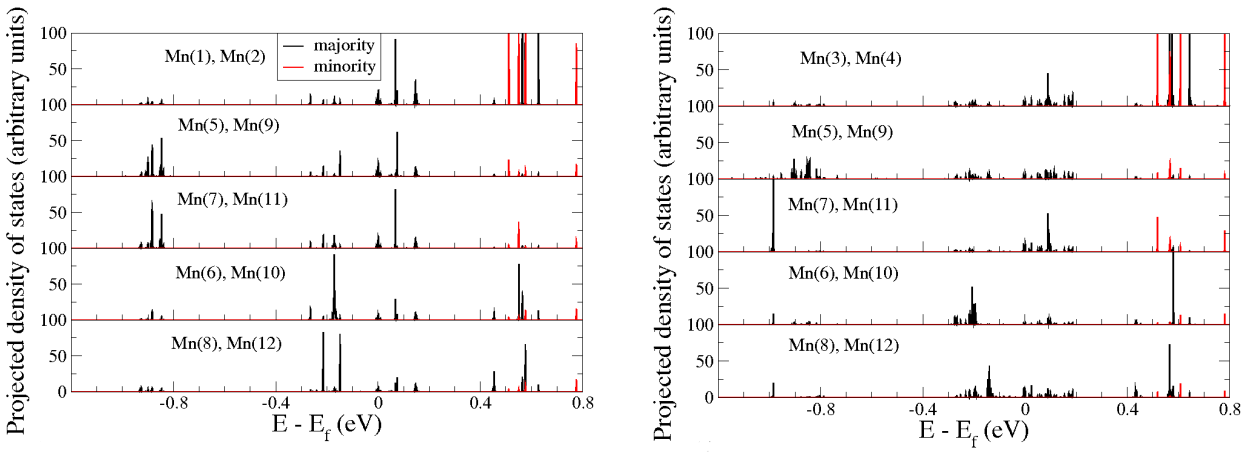


FIG. 8: (Color online) Spin-polarized DOS projected onto the Mn $d$ orbitals for (a) Geo 1:Au-$(SC_3H_6)_2$-hollow and (b) Geo 1:Au-$(C_3H_6)_2$: majority-spin (black) and minority-spin (red). Refer to Fig. 2 for numbering of the Mn ions. The DOS projected onto the Mn(1) and Mn(2) sites are similar to those onto the Mn(3) and Mn(4) sites.

geometries with the orientation (1) provide somewhat a higher current than those with the orientation (2). However, if one can arrange the transport to occur through the HOMO level (by application of gate voltage to the $Mn_{12}$), geometries in the orientation (2) will give a much higher current than those in the orientation (1). One caveat is that for a short distance $d$ the size of the $Mn_{12}$ prohibits interface geometries with the orientation (1) from being formed.

For all of the geometries considered, the effect of spin filtering remains robust. The spin-filtering effect occurs in the transport through the $Mn_{12}$ because its majority-spin HOMO and LUMO levels are well separated from the minority-spin HOMO and LUMO levels and because the minority-spin HOMO level is located sufficiently below the majority-spin HOMO level (Fig. 2 in Ref.[15], Figs. 8, 9, and 10). This feature of the HOMO and LUMO does not change with interface geometry. However, the degree of the spin filtering depends on molecular orientations, bonding types, and the distance $d$. We first compare the spin-filtering effect for the geometries in the orientation (1) to that in the orientation (2). Figure 11 shows the spin-polarized $T(E,0)$ for six geometries [Fig. 2(a), (c), (d), (e), (h), and (i)]. In the last column of Table 1, the ratio of the majority-spin to the minority-spin transmission coefficients at the energy level associated with the LUMO level, $(T_\uparrow - T_\downarrow)/T_\downarrow$, is provided. For the geometries in the orientation (1), the ratio varies from $6.11\times10^6$ to $5.26\times10^8$, while

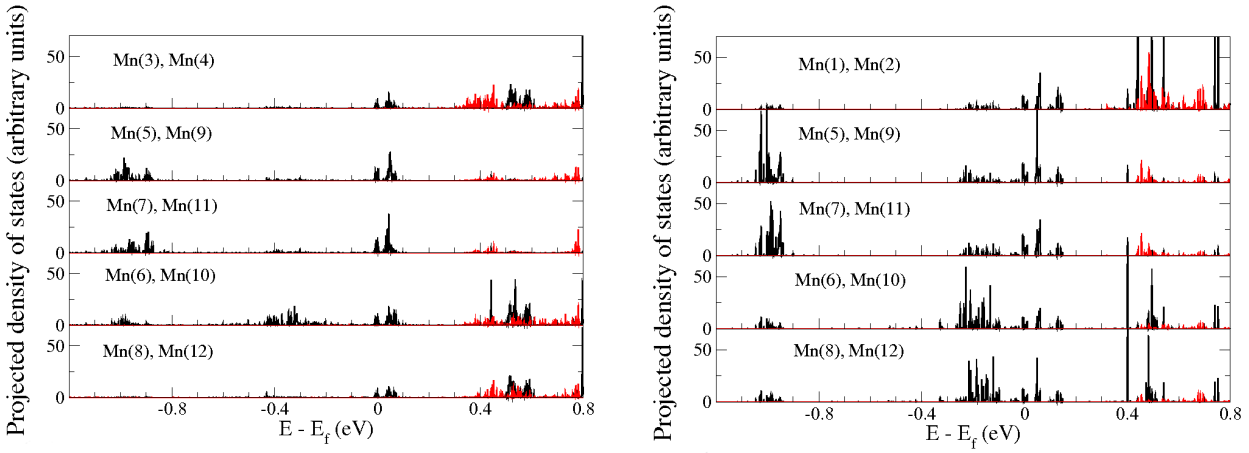


FIG. 9: (Color online) Spin-polarized DOS projected onto the Mn $d$ orbitals for (a) Geo 2:Au-$S_4$ and (b) Geo 2:Au-H-no-linker: majority-spin (black) and minority-spin (red). Refer to Fig. 2 for numbering of the Mn ions. The DOS projected onto the Mn(1) and Mn(2) sites are similar to those onto the Mn(3) and Mn(4) sites.

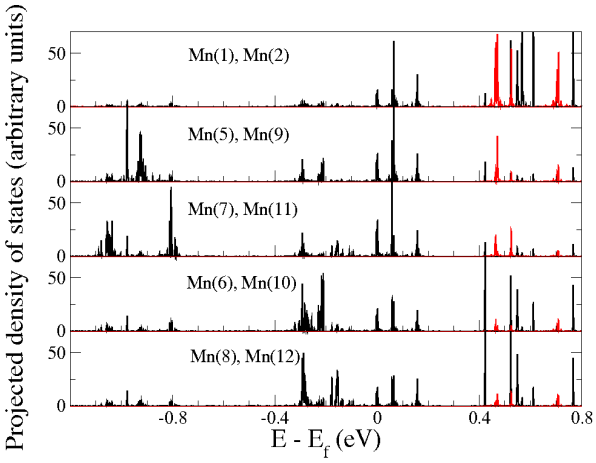


FIG. 10: (Color online) Spin-polarized DOS projected onto the Mn $d$ orbitals for Geo 2:Au-$(SC_2H_4)_4$: majority-spin (black) and minority-spin (red). Refer to Fig. 2 for numbering of the Mn ions. The DOS projected onto the Mn(1) and Mn(2) sites are similar to those onto the Mn(3) and Mn(4) sites.

for those in the orientation (2), the ratio is in the range of $7.39\times10^2$ to $2.86\times10^5$. A larger spin-filtering effect is obtained for the geometries in the orientation (1) than for those in the orientation (2). This is partly because the linker molecules in the orientation (2) are in a closer proximity to the Mn(1), Mn(2), Mn(3), and Mn(4) sites than those in the orientation

(1). These four Mn sites mainly contribute to the minority-spin density of states as shown in Figs. 8 and 9. Due to this proximity of the four Mn sites, the minority-spin DOS for the geometries in the orientation (2) is more spread than that for the geometries in the orientaion (1). An additional reason is as follows. As discussed earlier and shown in Figs. 8, 9, and 10, the LUMO arises from the majority-spin Mn $d$ orbitals. At the energy level where the ratio is obtained, the majority-spin transmission is of the order of unity, independent of the distance $d$, because the transport is carried by the LUMO level. However, at that energy level, the transport of minority-spin electrons is in the tunneling regime, since there are no corresponding molecular levels of the minority-spin. Thus, the minority-spin transmission decreases exponentially with $d$. Since the geometries in the orientation (1) have much longer distances $d$ than those in the orientation (2), the coefficients of the minority-spin transmission for the former geometries are much smaller than those for the latter geometries. This renders the greatly enhanced ratio for the geometries in the orientation (1). Now let us briefly discuss the influence of bonding type on the spin-filtering effect. For the orientation (1) the minority-spin DOS for the Au-C bonding is slightly broader than that for the Au-S bonding [compare Fig. 8(a) to (b)]. Thus, the ratio for the Au-C bonding is lower than that for the Au-S bonding (Table 1) for a given distance $d$. Similarly, for the orientation (2), the minority-spin DOS for the Au-S bonding is more delocalized than that for the Au-H bonding [compare Fig. 9(a) to (b)]. So the ratio for the Au-S bonding is lower than that for the Au-H bonding for a given distance $d$. For a specific bonding type, the ratio increases with increasing the distance $d$ because of the reason explained above. For example, for the Au-S bonding, the minority-spin PDOS for Geo 2:Au-$(SC_2H_4)_4$ is much more localized than that for Geo 2:Au-$S_4$ [compare Fig. 10 to 9(a)]. Thus, the ratio for the former is two orders of magnitude greater than that for the latter. Additionally, we note from Figs. 4 and 11 that this ratio, $(T_\uparrow - T_\downarrow)/T_\downarrow$, remains in the range of 100 to $10^7$ even at the energy level where the transport of both the majority spin and the minority spin is in the tunneling regime. The spin-filtering effect may be achieved for other SMMs with high magnetic moments and stable ground-state spin multiplets.

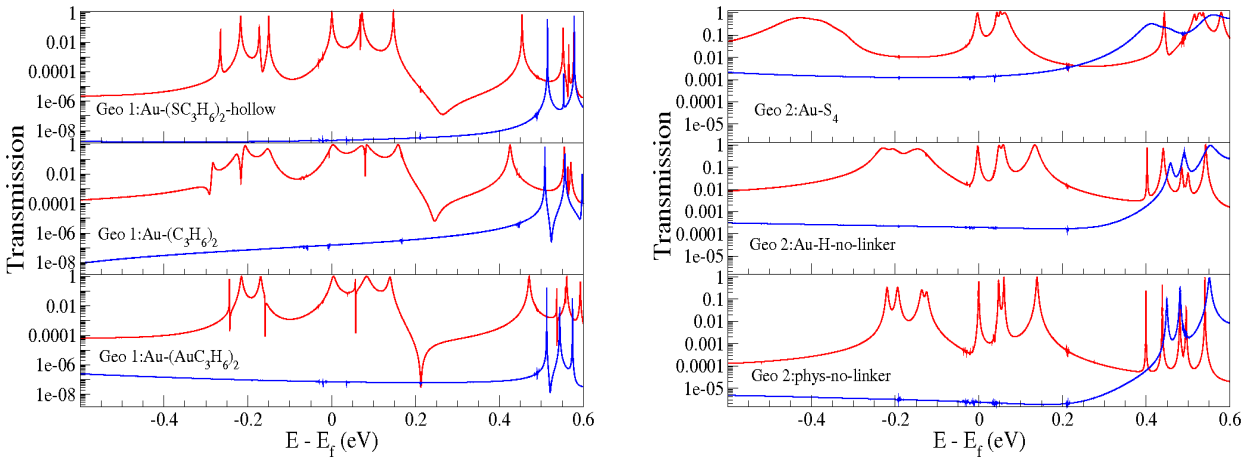


FIG. 11: (Color online) Spin-polarized transmission at zero bias with a logarithmic scale in the vertical axis. Majority-spin contribution: red, minority-spin contribution: blue. The vertical scales of the figures on the left differ from those on the right.

### D. Effect of bonding type and linker group

We investigate the effect of binding site on transport properties for a given bonding type, for example, the Au-S bonding in the orientation (1), Geo 1:Au-$(SC_3H_6)_2$. We consider hollow and on-top binding sites of the S atoms to the Au surface in that geometry, without geometry relaxation. The broadening of the LUMO level somewhat decreases from the hollow-site to the on-top geometries, while the broadening of the HOMO level slightly increases (Table 1). This difference in the broadening is much smaller than that induced by different bonding types. Despite this small difference, the overall features of $T(E, 0)$ for the two geometries are fairly similar to each other, as shown in Fig. 4(a). Thus, the $I$-$V$ curve for the on-top site geometry is expected to be similar to that for the hollow-site geometry, Geo 1:Au-$(SC_3H_6)_2$-hollow, shown in Fig. 5.

We compare the transport properties of the geometries with three bonding types in the orientation (1), where the distance $d$ is fairly similar to one another: Au-C bonding [Geo 1:Au-$(C_3H_6)_2$], Au-S bonding [Geo 1:Au-$(SC_3H_6)_2$-hollow], and Au-Au bonding [Geo 1:Au-$(AuC_3H_6)_2$]. The broadening of the LUMO level for the geometry with the Au-C bonding is one order of magnitude larger than that with the Au-S bonding, and it is twice as large as that with the Au-Au bonding, as shown in Figs. 4(a) and 7. Accordingly, the current for the Au-C bonding at 50 mV is one order of magnitude higher than that for the Au-S

bonding, and is twice as high as that for the Au-Au bonding (Fig. 5). Among all of the interface geometries considered, for a fixed distance $d$, the geometry with the Au-C bonding reveals the largest broadening of the LUMO level, leading to the largest current (Fig. 5).

To understand the nature of the bonding between the linker molecules and the electrodes, we compute the density of states projected onto the $p$ orbitals of the S or C atoms of the linker molecules closest to the electrodes, and onto the $s$ orbitals of the three Au surface atoms closest or bonded to those S or C atoms. The DOS projected onto the Au $s$ orbitals change with interface geometries due to the interactions between the linker molecules and the electrodes. For Geo 1:Au-$(C_3H_6)_2$, only the $p_z$ orbitals of the C atoms of the linker group greatly overlap with the Au $s$ orbitals of the electrodes near $E_f$ [the bottom four panels of Fig. 12(a)]. The density of the LUMO coincides with the peaks in the region bound by the dashed lines in Fig. 12(a). Strong overlap (in terms of the peak height and the width of the region) among the Au $s$ orbitals, the C $p$ orbitals, and the LUMO results in a high current through the $Mn_{12}$. For Geo 1:Au-$(SC_3H_6)_2$-hollow, the $p_x$, $p_y$, and $p_z$ orbitals of the S atoms have much weaker overlap with the Au $s$ orbitals in the region where the LUMO appears (confined by the dashed lines) than the Au-C bonding case [the top four panels of Fig. 12(a)], which gives rise to a reduced transmission probability. For Geo 2:Au-$S_4$, only the $p_x$ and $p_y$ orbitals of the S atoms bear some overlap with the Au $s$ orbitals near $E_f$ (in the region bound by the dashed lines) [the top four panels of Fig. 12(b)]. This overlap is weaker than that for the Au-C bonding but stronger than that for Geo 1:Au-$(SC_3H_6)_2$-hollow or for Geo 2:Au-$(SC_2H_4)_4$ [the bottom four panels of Fig. 12(b)]. This tendency agrees well with the trend in the value of $\Gamma_{\rm LUMO}$ and the current. Additionally, our calculated spatially resolved density of states of the LUMO [Fig. 6(a)] uncovers that the geometry with the Au-C bonding gives rise to larger density in the linker molecules than any other geometries considered. Thus, the transmission probability is highest for the geometry with the Au-C bonding. The geometries with the Au-S bonding do not have as high transmission probabilities as that for the Au-C bonding or the Au-Au bonding. Consequently, the Au-C bonding provides the highest current and the Au-S bonding gives rise to a lower current than the Au-C bonding or the Au-Au bonding.

We discuss the transport properties of the geometries with physisorption and without linker molecules. One of the geometries without linker molecules, Geo 2:Au-H-no-linker, has the shortest distance $d$ among the geometries considered. The broadening of the LUMO level

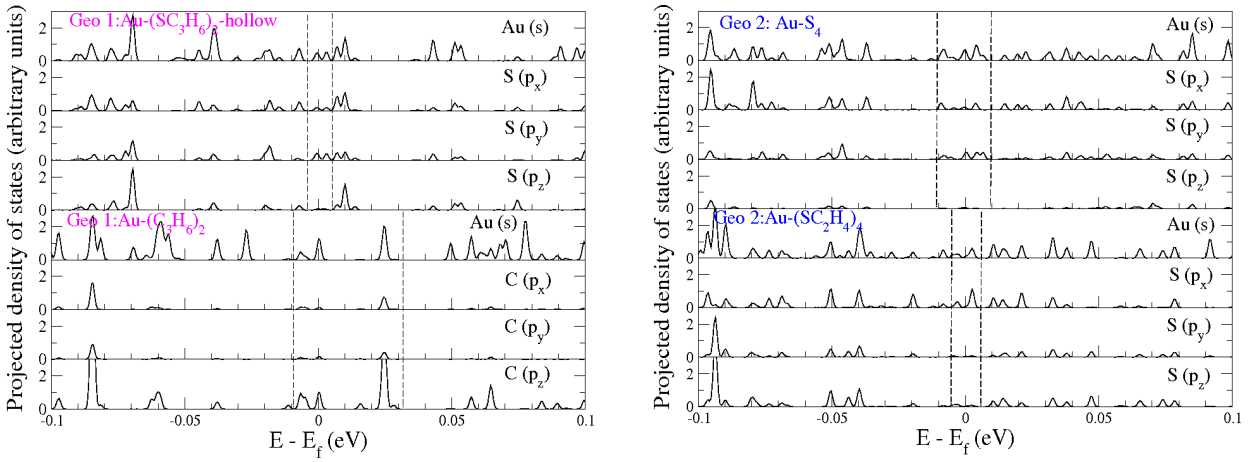


FIG. 12: Majority-spin DOS projected onto the $s$ orbitals of the three Au surface atoms and $p_x$, $p_y$, $p_z$ orbitals of the S or C atom closest or bonded to the Au atoms for (a) Geo 1:Au-$(SC_3H_6)_2$-hollow and Geo 1:Au-$(C_3H_6)_2$, and (b) Geo 2:Au-$S_4$ and Geo 2:Au-$(SC_2H_4)_4$. In the region confined by the dashed lines, the density peaks overlap with the LUMO. The vertical scale in this figure differs from those in Figs. 3 and 7.

for that geometry is 54% of that with the shortest Au-S bonding (Geo 2:Au-$S_4$), and it is 21% of that with the Au-C bonding, as shown in Table 1. The current for the geometry with the Au-H bonding at 50 mV is 44% of that for Geo 2:Au-$S_4$, and it is 36% of that with the Au-C bonding (Fig. 5). In the case of physisorption, with the fixed distance $d$, the broadening of the LUMO level for Geo 2:phys-no-linker is the same as that for Geo 2:phys-$(CH_3)_4$. This implies that the alkane chains do not play a role in the broadening of the LUMO level. For the given distance $d$, the broadening of the LUMO level for these two physisorbed geometries takes up only 15% of that for the Au-S bonding (Geo 2:Au-$S_4$), as listed in Table 1. Yet, the current for Geo 2:phys-$(CH_3)_4$ at 50 mV is two orders of magnitude lower than that for Geo 2:Au-$S_4$ (Fig. 5). Thus, in this case, the ratio of the values of $\Gamma_{\rm LUMO}$ for the two geometries does not have the same order as the ratio of the corresponding currents. The discrepancy between the two ratios arises from the difference in the response of the junctions or in the changes of the transmission with bias voltage. Notice that Fig. 4 shows the transmission spectra for zero bias. For chemisorbed junctions the molecular orbitals strongly overlap with the orbitals of the electrodes. Thus, when bias voltage is applied, this overlap is enhanced especially in the regions between adjacent transmission peaks. However, for physisorbed junctions, the transmission peaks remain sharp even with bias voltage because of no overlap

of the molecular orbitals with the orbitals of the electrodes. A combination of this effect with the ratio of the values of $\Gamma_{\rm LUMO}$ explains the ratio of the current through Geo 2:phys-$(CH_3)_4$ to that through Geo 2:Au-$S_4$. Our overall comparison of the transport behavior among different bonding types summarizes that the current through the $Mn_{12}$ decreases in the following order, for a given distance $d$: Au-C, Au-Au, Au-S, Au-H, and physisorption.

## IV. CONCLUSION

We simulated a single-molecule junction based on the SMM $Mn_{12}$ connected to Au(111) electrodes via five different bonding mechanisms and two molecular orientations, and calculated their transport properties, using the non-equilibrium Green's function method and the spin-polarized DFT. Geometry relaxation of the junction renders a small decrease in the electric current at low bias voltage. If the electron transport is carried by the LUMO (HOMO) level of the $Mn_{12}$, geometries in the orientation (1) provide a higher (lower) current that those in the orientation (2). This is due to the structure of the $Mn_{12}$. Our two-terminal transport calculations reveal that the LUMO level is relevant to the transport through the $Mn_{12}$. In all of the interface geometries considered, the spin-filtering effect discussed in Ref. [14] remains robust, and it may occur to some other SMMs where the ground-state spin is large and the ground-state spin multiplet is reasonably well separated in energy from the low-lying excited spin multiplets. Some experimental studies[4,5,10,11] show that upon deposition of $Mn_{12}$ molecules on an Au surface, the valence states of all of the Mn ions are preserved, while some other experimental works[8,9,12] reveal that such a deposition induces changes in the valence states of some of the Mn ions. In cases where such changes do not occur[4,5,10,11], the spin-filtering effect is expected. We also find that the current through the $Mn_{12}$ depends on a bonding type and that it decreases in the following order for a fixed $d$: Au-C, Au-Au, Au-S, Au-H, and physisorption. This is because the overlap among the LUMO, the S or C $p$ orbitals from the linker molecules, and the $s$ orbitals of the Au surface atoms, decreases in that order. The degeneracy in the magnetic levels of the $Mn_{12}$ for a given spin $S$ is lifted by spin-orbit coupling. Then inelastic transport through low-energy spin excitations must be included for quantitative comparison to experimental data. However, the general trend in the transport as a function of bonding type and interface geometry found in this study may still hold.

**Acknowledgments**

K.P. is supported by NSF DMR-0804665 and the Jeffress Memorial Trust Funds. V.M.G.S. thanks the Spanish Ministerio de Ciencia e Innovación for a Juan de la Cierva fellowship and the Marie Curie European ITNs FUNMOLS and NANOCTM for funding. J.F. is supported by MEC FIS2006-12117. Computational support was provided by the SGI Altix Linux Supercluster (Cobalt) and Intel 64 Cluster (Abe) at the National Center for Supercomputing Applications under DMR060011 and by Virginia Tech Linux clusters and Advanced Research Computing.

---

[1] H. B. Heersche, Z. de Groot, J. A. Folk, H. S. van der Zant, C. Romeike, M. R. Wegewijs, L. Zobbi, D. Barreca, E. Tondello, and A. Cornia, Phys. Rev. Lett. **96**, 206801 (2006)

[2] M.-H. Jo, J. E. Grose, K. Baheti, M. M. Deshmukh, J. J. Sokol, E. M. Rumberger, D. N. Hendrickson, J. R. Long, H. Park, and D. C. Ralph, Nano Lett. **6**, 2014 (2006).

[3] J.J. Henderson, C.M. Ramsey, E. del Barco, A. Mishra, and G. Christou, J. Appl. Phys. **101**, 09E102 (2007).

[4] M. Burgert, S. Voss, S. Herr, M. Fonin, U. Groth, and U. Rudiger, J. Am. Chem. Soc. **129**, 14362 (2007).

[5] S. Voss, O. Zander, M. Fonin, U. Rudiger, M. Burgert, and U. Groth, Phys. Rev. B **78**, 155403 (2008).

[6] L. Bogani, C. Danieli, E. Biavardi, N. Bendiab, A. L. Barra, E. Dalcanale, W. Wernsdorfer, and A. Cornia, Ang. Chem.-Int. Ed. **48**, 746 (2009).

[7] Z. Salman, K. H. Chow, R. I. Miller, A. Morello, T. J. Parolin, M. D. Hossain, T. A. Keeler, C. D. P. Levy, W. A. MacFarlane, G. D. Morris, H. Saadaoui, D. Wang, R. Sessoli, G. G. Condorelli, and R. F. Kiefl, Nano Lett. **7**, 1551 (2007).

[8] L. Zobbi, M. Mannini, M. Pacchioni, G. Chastanet, D. Bonacchi, C. Zanardi, R. Biagi, U. del Pennino, D. Gatteschi, A. Cornia, and R. Sessoli, Chem. Commun. (Cambridge) **12**, 1640 (2005).

[9] U. del Pennino, V. D. Renzi, R. Biagi, V. Corradini, L. Zobbi, A. Cornia, D. Gatteschi, F. Bondino, E. Magnano, M. Zangrando, M. Zacchigna, A. Lichteinstein, and D. W. Boukhvalov,

Surf. Sci. **600**, 4185 (2006).

[10] S. Voss, M. Fonin, U. Rudiger, M. Burgert, U. Groth, and Y. S. Dedkov, Phys. Rev. B **75**, 045102 (2007).

[11] G. Otero, E. Evangelio, C. Rogero, L. Vazquez, J. Gomez-Segura, J. A. M. Gago, D. Ruiz-Molina, Langmuir, **25**, 10107 (2009).

[12] M. Mannini, F. Pineider, P. Sainctavit, L. Joly, A. Fraile-Rodriguez, M.-A. Arrio, C. C. dit Moulin, W. Wernsdorfer, A. Cornia, D. Gatteschi, and R. Sessoli, Adv. Mat. **21**, 167 (2009).

[13] M. Mannini, F. Pineider, P. Sainctavit, C. Danieli, E. Otero, C. Sciancalepore, A. M. Talarico, M.-A. Arrio, A. Cornia, D. Gatteschi, and R. Sessoli, Nat. Mat. **8**, 194 (2009).

[14] S. Barraza-Lopez, K. Park, V. García-Suárez, and J. Ferrer, J. Appl. Phys. **105**, 07E309 (2009).

[15] S. Barraza-Lopez, K. Park, V. García-Suárez, and J. Ferrer, Phys. Rev. Lett. **102**, 246801 (2009).

[16] C. D. Pemmaraju, I. Rungger, and S. Sanvito, Phys. Rev. B **80**, 104422 (2009).

[17] L. Michalak, C. M. Canali, M. R. Pederson, V. G. Benza, M. Paulsson, arXiv:0812.1058.

[18] W. Liang, M. P. Shores, M. Bockrath, J. R. Long, and H. Park, Nature **417**, 725 (2002).

[19] J. Park, A. N. Pasupathy, J. I. Goldsmith, C. Chang, Y. Yaish, J. R. Petta, M. Rinkoski, J. P. Sethna, H. D. Abruña, P. L. McEuen, and D. C. Ralph, Nature **417**, 722 (2002).

[20] B. Xu and N. J. Tao, Science **301**, 1221 (2003).

[21] H. Basch, R. Cohen, and M. A. Ratner, Nano Lett. **5**, 1668 (2005).

[22] L. Venkataraman, J. E. Klare, I. W. Tam, C. Nuckolls, M. S. Hybertsen, and M. L. Steigerwald, Nano Lett. **6**, 458 (2006).

[23] L. Venkataraman, J. E. Klare, C. Nuckolls, M. S. Hybertsen, and M. L. Steigerwald, Nature **442**, 904 (2006)

[24] X. Li, J. He, J. Hihath, B. Xu, S. M. Lindsay, and N. Tao, J. Am. Chem. Soc. **128**, 2135 (2006).

[25] D. Millar, L. Venkataraman, and L. H. Doerrer, J. Phys. Chem. C **111**, 17635 (2007).

[26] J. M. Beebe, V. B. Engelkes, L. L. Miller, and C. D. Frisbie, J. Am. Chem. Soc. **124**, 11268 (2002).

[27] M. Kiguchi, O. Tal, S. Wohlthat, F. Pauly, M. Krieger, D. Djukic, J. C. Cuevas, and J. M. van Ruitenbeek, Phys. Rev. Lett. **101**, 046801 (2008).

[28] O. Tal, M. Kiguchi, W. H. A. Thijssen, D. Djukic, C. Untiedt, R. H. M. Smit, and J. M. van Ruitenbeek, Phys. Rev. B **80**, 085427 (2009).

[29] J. Ferrer and V. M. García-Suárez, Phys. Rev. B **80**, 085426 (2009).

[30] T. Lis, Acta Crystallogr. B **36**, 2042 (1980).

[31] K. Park, M. R. Pederson, and C. S. Hellberg, Phys. Rev. B **69**, 014416 (2004)

[32] J. R. Friedman, M. P. Sarachik, J. Tejada, and R. Ziolo, Phys. Rev. Lett. **76**, 3830 (1996); L. Thomas and F. Lionti and R. Ballou and D. Gatteschi and R. Sessoli and B. Barbara, Nature, **383**, 145 (1996).

[33] A. L. Barra, D. Gatteschi, and R. Sessoli, Phys. Rev. B **56**, 8192 (1997).

[34] S. Hill, J. A. A. J. Perenboom, N. S. Dalal, T. Hathaway, T. Stalcup, and J. S. Brooks, Phys. Rev. Lett. **80**, 2453 (1998).

[35] V. M. García-Suárez, A. R. Rocha, S. W. Bailey, C. J. Lambert, S. Sanvito, and J. Ferrer, Phys. Rev. Lett. **95**, 256804 (2005).

[36] A.R. Rocha, V.M. García-Suárez, S. Bailey, C. Lambert, J. Ferrer, and S. Sanvito, Phys. Rev. B **73**, 085414 (2006).

[37] L. Fernández-Seivane, M. A. Oliveira, S. Sanvito, and J. Ferrer, J. Phys.: Condens. Matter **18**, 7999 (2006).

[38] J. M. Soler, E. Artacho, J. D. Gale, A. García, J. Junquera, P. Ordejn, and D. Snchez-Portal, J. Phys.: Condens. Matter **14**, 2745 (2002); J. Junquera, Ó. Paz, D. Sánchez-Portal and E. Artacho, Phys. Rev. B **64**, 235111 (2001); P. Ordejón, D. A. Drabold, M. P. Grumbach and R. M. Martin, Phys. Rev. B **51**, 1456 (1995).

[39] J. P. Perdew, K. Burke, and M. Ernzerhof, Phys. Rev. Lett. **77**, 3865 (1996).

[40] N. Troullier and J. L. Martins, Phys. Rev. B **43**, 1993 (1991).

[41] J. Junquera, O. Paz, D. Sánchez-Portal, and E. Artacho, Phys. Rev. B **64**, 235111 (2001).

[42] M. R. Pederson and S. N. Khanna, Phys. Rev. B **60**, 9566 (1999).

[43] S. Barraza-Lopez, M. C. Avery, and K. Park, Phys. Rev. B **76**, 224413 (2007).

[44] S. Barraza-Lopez, M. C. Avery, and K. Park, J. Appl. Phys. **103**, 07B907 (2008).

[45] G. Kresse and J. Furthmüller, Phys. Rev. B **54**, 11169 (1996); G. Kresse and J. Furthmüller, Comp. Mat. Sci. **6**, 15 (1996).

[46] S. Sanvito, C. J. Lambert, J. H. Jefferson, and A. M. Bratkovsky, Phys. Rev. B **59**, 11936 (1999).

[47] S. M. Gruenbaum, M. H. Henney, S. Kumar, and S. Zou, J. Phys. Chem. B **110**, 4782 (2006).

[48] D. L. DuBose, R. E. Robinson, T. C. Holovics, D. R. Moody, E. C. Weintrob, C. L. Berrie, and

M. V. Barybin, Langmuir **22**, 4599 (2006).

[49] D. W. Boukhvalov, M. Al-Saqer, E. Z. Kurmaev, A. Moewes, V. R. Galakhov, L. D. Finkelstein, S. Chuizbaian, M. Neumann, V. V. Dobrovitski, M. I. Katsnelson, A. I. Lichtenstein, B. N. Harmon, K. Endo, J. M. North, and N. S. Dalal, Phys. Rev. B **75**, 014419 (2007).

[50] H. J. Eppley, H.-L. Tsai, N. de Vries, K. Folting, G. Christou, and D. N. Hendrickson, J. Am. Chem. Soc. **117**, 301-317 (1995); M. Soler, W. Wernsdorfer, K. A. Abboud, J. C. Huffman, E. R. Davidson, D. N. Henrickson, and G. Christou, J. Am. Chem. Soc. **125**, 3576 (2003).

[51] R. Basler, A. Sieber, G. Chaboussant, H. Güdel, N. E. Chakov, M. Soler, G. Christou, A. Desmedt, and R. Lechner, Inorg. Chem. **44**, 649 (2005).

[52] S. Datta, *Electronic Transport in Mesoscopic Systems* (Cambridge University Press, 1995).

[53] S. Datta, Nanotechnology **15**, S433 (2004).

[54] J. M. Ziman, *Principles of the theory of solids*, 2nd Edition (Cambridge University Press, 1972).

[55] For Geo 2:Au-$S_4$, the broadening of the HOMO level of the $Mn_{12}$ is buried under the single broad transmission peak (width of 0.11 eV) associated with four molecular orbitals right below the Fermi level including the HOMO level. Thus, in order to compute $C_1$ and $C_2$ for the HOMO level, we assume that the value of $\Gamma_{\rm HOMO}$ is 0.11/4 eV.

TABLE I: Average broadening of the HOMO and LUMO levels ($\Gamma_{\rm HOMO}$, $\Gamma_{\rm LUMO}$) of the $Mn_{12}$ for the nine interface geometries. All geometries are optimized, unless stated otherwise. The broadening is calculated from zero-bias transmission spectra. The value of $\Gamma_{\rm HOMO}$ for Geo 2:Au-$S_4$ (Geo 2:Au-H-no-linker) is marked by † because it represents the full width at half maximum of the single broad transmission peak associated with the four (two) molecular levels right below $E_f$ including the HOMO level, as shown in Fig. 4(b). The ratio of the majority-spin to the minority-spin transmission, $(T_\uparrow - T_\downarrow)/T_\downarrow$, is computed at the energy level corresponding to the LUMO level.

| interface geometry (orientation, linker group) | bonding type binding site | $d$ (Å) | Fig. 1 | $\Gamma_{\rm LUMO}$ (eV) | $\Gamma_{\rm HOMO}$ (eV) | $(T_\uparrow - T_\downarrow)/T_\downarrow$ |
|---|---|---|---|---|---|---|
| Geo 1:Au-$(SC_3H_6)_2$-hollow initial geometry | Au-S, hollow | 25.73 | N/A | 0.0028 | $2.6\times10^{-5}$ | $2.57\times10^{8}$ |
| Geo 1:Au-$(SC_3H_6)_2$-ontop initial geometry | Au-S, on-top | 25.73 | (b) | 0.0020 | $3.4\times10^{-5}$ | $5.26\times10^{8}$ |
| Geo 1:Au-$(SC_3H_6)_2$-hollow | Au-S, hollow | 25.73 | (a) | 0.0020 | 0.00050 | $4.37\times10^{8}$ |
| Geo 1:Au-$(C_3H_6)_2$ | Au-C, on-top | 23.33 | (c) | 0.020 | 0.020 | $6.11\times10^{6}$ |
| Geo 1:Au-$(AuC_3H_6)_2$ | Au-Au, hollow | 25.73 | (d) | 0.0090 | 0.0028 | $1.40\times10^{7}$ |
| Geo 2:Au-$S_4$ | Au-S, hollow | 14.48 | (e) | 0.0078 | $0.11^\dagger$ | $7.39\times10^{2}$ |
| Geo 2:Au-$(SC_2H_4)_4$ | Au-S, hollow | 19.01 | (f) | 0.0040 | 0.016 | $2.86\times10^{5}$ |
| Geo 2:phys-$(CH_3)_4$ | physisorption | 14.56 | (g) | 0.0010 | 0.0032 | $2.32\times10^{5}$ |
| Geo 2:Au-H-no-linker | Au-H, on-top | 12.69 | (h) | 0.0042 | $0.054^\dagger$ | $4.63\times10^{3}$ |
| Geo 2:phys-no-linker | physisorption | 14.48 | (i) | 0.0011 | 0.0092 | $2.74\times10^{5}$ |